

On the preferred length scale in the anisotropy field of extragalactic IRAS sources

R. Fabbri¹ and V. Natale²

¹ Dipartimento di Fisica dell'Università, Sezione di Fisica Superiore, Via S. Marta 3, I-50139 Firenze, Italy

² CAISMI-CNR, Largo Fermi 5, I-50125 Firenze, Italy

Received ; accepted

Abstract. We investigate the existence and meaning of a preferred length in the large-scale distribution of 60- μ m IRAS sources applying three tests to the 2-dimensional distribution on the celestial sphere, involving respectively the rms fluctuation and the correlation function of the source number density, and the peak number statistics. For HDM models we find a best value $\lambda_0 = 45 - 55 h^{-1}$ Mpc for the peak of the spectral function $P(k)$, close to the preferred wavelength $\lambda = 30 - 40 h^{-1}$ Mpc of naïve single-scale perturbation models. A feature should indeed be generated in this range by the anticorrelation region of $\xi(r)$, although it is not detected by recent Fourier transform analyses of redshift catalogs. Our tests provide acceptable fits for CDM models with either $\Omega_0 h = 0.3 - 0.5$ or $\Omega_0 h = 0.1 - 0.2$, in agreement with results in current literature. However, the quality of such fits is less satisfactory than for HDM models, with the exception of the peak number statistics, and we are not able to find a parameter interval satisfying all of our tests simultaneously. These results may indicate that the cosmic spectrum is more complicated than the smooth shapes predicted by current theoretical models.

Key words: cosmology – infrared sources

1. Introduction

The anisotropy field in the 2-dimensional distribution of IRAS sources on angular scales of $1^\circ - 70^\circ$ was recently used to derive a characteristic length scale of about $50h^{-1}$ Mpc (Fabbri & Natale 1993; the Hubble constant H_0 is here $100h \text{ km s}^{-1} \text{ Mpc}^{-1}$), significantly larger than the dipole-dominating scale (Villumsen & Strauss 1987; Clowes et al. 1987) and comparable to the distance $D_0 \approx 30h^{-1}$ Mpc at which the galaxy-galaxy correlation function $\xi(r)$ becomes negative (Guzzo et al. 1991; see also

Davis & Peebles 1983). Torres et al. (1994) have shown that the Fourier transform of $\xi(r)$, suitably modeled to reproduce the data of Guzzo et al., should induce a peak in the spectral function $P(k)$ of the inhomogeneities at a wavelength $\lambda_{\text{peak}} \simeq 1.5D_0$; further, they find that best fitting on COBE data, involving the angular correlation function of the cosmic background radiation, provides $\lambda_{\text{peak}} = 51 \pm 18 h^{-1}$ Mpc. We are thereby lead to suspect that the characteristic length in IRAS may be close to a peak of $P(k)$, although not necessarily to its absolute maximum. This interpretation, even in its weakest form, seems to be not consistent with several works inferring $P(k)$ from the 3-dimensional distributions of visible and IR galaxies and clusters (Vogeley et al. 1992; Fisher et al. 1993; Einasto et al. 1993; Jing & Valdarnini, 1993). These works, based on Fourier transforms of redshift-space distributions, provided spectra which, although not completely consistent with each other, steadily increase up to or beyond $100h^{-1}$ Mpc: When some peak is detected, it is located at large wavelengths, in the range $180 - 300 h^{-1}$ Mpc. However, Bahcall et al. (1993) argue that large-scale velocities induced by the inhomogeneity field itself, not properly taken into account in the above works, may lead to largely overestimate the large-scale portion of the spectrum in real (rather than redshift) space. Corrections are strongly model dependent, and for some of the CDM models considered by Bahcall et al. they shift the peak wavelengths in the IRAS and CfA spectra down to $\simeq 100h^{-1}$ Mpc. Is it thereby important in our view to exploit alternative techniques that are not affected by the problem of large scale velocities.

In this paper we reconsider the question of the significance and reliability of the preferred scale that we identified in Version I of the IRAS Point Source Catalog. We use a larger sample including 12511 sources derived from Version II of the Catalog, and we perform three statistical tests based on finite-size bins. These include the shapes of the functions (i) $\Delta N_{\text{rms}}(\gamma, \gamma)$, the rms fluctuation in the source number density vs. angular scale γ in the range

Send offprint requests to: R.Fabbri

$1^\circ - 72^\circ$, (ii) $C(\gamma, \sigma)$, the autocorrelation function of the number density at $2^\circ - 25^\circ$, and (iii) $N_{\text{peak}}(\sigma, T)$, the number of local maxima in the source distribution vs. Gaussian beam dispersion σ (in the range $1^\circ - 10^\circ$) and peak-height threshold T . The experimental data are tested against a large number (about 2000) of theoretical models.

First we model the inhomogeneity field by isotropically stochastic perturbations endowed with a single wavelength λ , and search for the best values of λ , the cosmological density parameter Ω_0 , and the product bV (the biasing factor of IRAS sources times the local velocity). Although the present sample allows us detecting some dependency of λ on the chosen angular range (in particular using the statistics on N_{peak}), nevertheless we can identify a preferred range around $30 - 40 h^{-1}$ Mpc, irrespective of Ω_0 which cannot be determined by the present tests. We then examine continuous spectra modeling both hot and cold matter with the usual requirement that $P(k) \propto k$ at large wavelengths. We find that the HDM model in the $\Omega_0 = 1$ cosmology gives excellent fits for all of our tests, except for one data point of ΔN_{rms} at the largest scale 71.7° . The HDM peak wavelength λ_0 is only slightly larger than λ found for single-scale models. Individual tests can give best values as high as $60 h^{-1}$ Mpc with large error bars, but two joint tests combining the peak number data with rms fluctuation and correlation function data, respectively, give $\lambda_0 = 52.5^{+22}_{-7} h^{-1}$ Mpc and $45.0^{+5}_{-1.5} h^{-1}$ Mpc. Although we cannot derive stringent limits on bV from individual HDM tests, when we require to simultaneously satisfy all of our tests we get a preferred value of $450 - 550$ km/s (in close agreement with results that we find from single-scale models for $\Omega_0 = 1$).

Basically the same picture arises for other sharply-peaked spectral forms, for which the only important parameter is the location λ_0 of the peak of $P(k)$. Thus similar results for λ_0 are found for simple two-power spectra with slopes around -1.5 at large k . The investigation of CDM models on the other hand provides a quite different picture. For individual tests we find best-fit values of the shape parameter $\Omega_0 h$ in one of the ranges $0.3 - 0.5$ or $0.1 - 0.2$. Low-density models are favoured by several studies (e.g., Efstathiou et al. 1992). Now for $\Omega_0 h \leq 0.5$ the peak wavelength is $\gtrsim 100 h^{-1}$ Mpc; in fact, single-scale models are quite unable to represent so broad spectra as those implied by CDM models. However, the quality of CDM fits is less satisfactory than for HDM models, with the exception of the peak number statistics. In addition, no range of $\Omega_0 h$ is completely satisfactory for all of our tests; this latter fact recalls the results of Scharf and Lahav (1993). It is well known that pure CDM models do not generally provide excellent fits to available data, a fact which motivates studies involving mixed matter (Davis et al. 1992, Taylor & Rowan-Robinson 1992) or a cosmological constant (Efstathiou et al. 1992). However, the comparison of HDM and CDM fits in our work (Sect. 4) is rather impressive.

The spectral window functions that can be suitably defined for $\Delta N_{\text{rms}}(\gamma, \gamma)$ and $C(\gamma, \sigma)$ show that such tests weight small scales less than other 2-dimensional tests from other authors (in particular, Scharf and Lahav 1993). This provides support to the idea that the preferred scale arising from sharply peaked spectra should correspond to something of physical. It is also clear that such a feature should be regarded as generated by the behaviour of $\xi(r)$ around $30 h^{-1}$ Mpc measured by Guzzo et al. (1991). Since we do not directly construct an explicit spectral form from data, we do not claim that our tests on the distribution of IRAS sources necessarily imply an absolute maximum of $P(k)$ at scale λ_0 , nor can we claim that HDM models satisfy the bulk of available astronomical data. However, our results make us believe that the shape of $P(k)$ below $100 h^{-1}$ Mpc should not be so simple and featureless as generally believed, and that a positive slope up to or beyond $180 h^{-1}$ Mpc is probably incorrect. According to recent measurements of the angular correlation function in the APM survey the spectrum rises above a power law around $30 h^{-1}$ Mpc and seems to be peaked at $100 h^{-1}$ Mpc (Baugh & Efstathiou 1993), a scale smaller than declared by most authors on the basis of redshift surveys. In our view the problem of the detailed shape of $P(k)$ is not so clearly solved and deserves further investigations.

2. Modelling

Our models assume that the large-scale inhomogeneities are described by a isotropic, Gaussian field of perturbations. The theory of source-count anisotropies has been developed (Fabbri 1988, 1992) for a Friedmann background with an arbitrary density parameter Ω_0 , perturbed by a cosmic density-wave spectrum $P(k)$ such that

$$\left\langle \left| \frac{\Delta \rho}{\rho} \right|^2 \right\rangle = \int dk k^2 P(k). \quad (1)$$

Here the dimensionless wavenumber k is connected to the physical wavelength by

$$k = \frac{2\pi c}{H_0 S(\Omega_0) \lambda}, \quad (2)$$

with $S(\Omega_0) = |1 - \Omega_0|^{\frac{1}{2}}$ for $\Omega_0 \neq 1$ and $S(1) = \frac{1}{2}$. All the quantities that will be evaluated theoretically are derived from the squared coefficients of a harmonic expansion of the source-count anisotropy field $\Delta N = \langle N \rangle \sum_{\ell m} a_{\ell m} Y_{\ell m}$. More precisely, we consider the expectation values

$$a_{\ell}^2 \equiv \sum_m \langle |a_{\ell m}|^2 \rangle = a_{S\ell}^2 + a_{N\ell}^2, \quad (3)$$

where we sum up the cosmic-structure contribution $a_{S\ell}^2$ given by

$$a_{S\ell}^2 = 4\pi (2\ell + 1) \int dk \frac{k^2 P(k)}{(k^2 - 4K)^2} A_{\ell}^2(k) \quad (4)$$

and the noise term $a_{N\ell}^2$ originated by discrete sources

$$a_{N\ell}^2 = \frac{(2\ell + 1)}{\langle N \rangle}. \quad (5)$$

In Eq. (4) K denotes the sign of space curvature and the functions $A_\ell(k)$ are suitable coefficients introduced by Fabbri (1988). We could also define window functions $\Psi_\ell(k)$ as in Scharf and Lahav (1993) by setting $A_\ell(k) \propto b(k^2 - 4K)\Psi_\ell(k)$, with b the biasing factor of IRAS sources.

The analysis of $A_\ell(k)$ (Fabbri 1992) shows that the source properties affect the calculation through the biasing factor, the luminosity function, the number evolution factor and, to a very small extent, the spectral index. We shall provide explicit results for the exponential-logarithmic luminosity function of Saunders et al. (1990), which best fits data with a number evolution factor $(1+z)^{3.7}$. However, using the double-power functions of Lawrence et al. (1986) or Villumsen and Strauss (1987) does not change the conclusions of Sect. 4 (adopting no source-number evolution of course, since they were obtained with this assumption). Since in any case the assumed source distribution extends farther than probed in redshift surveys (Strauss et al. 1990), we checked the influence of a cut-off placed at some z_{\max} . Figure 1 displays some typical results for a_ℓ^2 , showing that we get no significant differences provided $z_{\max} \gtrsim 0.1$. A sharp cutoff at redshifts $z_{\max} \lesssim 0.03$ would decrease the amplitude of high order harmonics relative to low order ones. Thus we just assume that sources still exist at a distance (along the light cone) equal to roughly three times the median depth of PSC. We do not regard this as an onerous requirement: In practice we only assume that the median depth of the catalog is determined by the source luminosity function and the lower flux limit. The global properties of the universe are involved through Ω_0 . Further, it was shown that, because of the presence of the discrete source term in Eq. (3), the shape of the harmonic spectrum of anisotropies depends both on the shape of $P(k)$ and on the product bV , with V the local velocity with respect to the cosmic background radiation. Since V is generated by the perturbation field itself, it is also a measure of the absolute normalization of $P(k)$. (This implies that the shape of a_ℓ^2 vs. ℓ should be sufficient to fix its own normalization.) However, V may be affected by nonlinear disturbances. On the other hand, the absolute normalization of a_ℓ^2 is affected by high redshift sources more than the shape of the harmonic spectrum (Fabbri 1988), and it might introduce a systematic error on the normalization of $P(k)$. We thereby prefer to fit bV and the normalization factor of $P(k)$ as two independent parameters. We then check a posteriori whether we obtain consistent results for $b\sigma_8$, the biased fluctuation in $8h^{-1}$ Mpc spheres, computed from these two parameters when they are both available. For the peak number test, only the first method (i.e., derivation from bV) can be used.



Fig. 1. The squared harmonic amplitudes vs. l for single-scale models with $\Omega_0 = 1$ and $h\lambda = 10$ and 90 Mpc. Full lines represent overlapping curves with $z_{\max} = 10^2$, 1 and 0.3 . Dashed lines refer to $z_{\max} = 0.1$, and the dotted one to $z_{\max} = 0.03$

As to the shape of $P(k)$, here we consider both single-scale models and continuous spectra. For the reasons outlined above, single-scale models only depend on three important parameters, i.e. λ , Ω_0 and bV . For a full investigation of their influence we generated a regularly spaced 'lattice' of 900 models for the adopted optimal set of source parameters [i.e., using the luminosity function of Saunders et al. (1990) and a mean spectral index of -1.395]; including also the luminosity functions of Lawrence et al. (1986) and Villumsen and Strauss (1987), we investigated about 1500 single-scale models. Continuous spectra, which were investigated only in conjunction with the exponential-logarithmic luminosity function, were modeled by simple analytic forms for hot and cold matter. HDM models are described by

$$P(k) \propto k \exp \left[-2 \left(\frac{k}{k_c} \right)^{\frac{3}{2}} \right], \quad (6)$$

with k_c the cutoff wavenumber. The peak wavelength is given by $\lambda_0 = 2 \cdot 3^{\frac{2}{3}} \pi c [H_0 S(\Omega_0) k_c]^{-1}$. The number of models computed with the spectrum in Eq. (6) was about 200, and we limited ourselves to the critical density cosmology. We also considered about 200 models with power-law behaviours at large k . We analyzed about 200 CDM models with

$$P(k) \propto k \left[1 + 1.7\tilde{k} + 9.0\tilde{k}^{\frac{3}{2}} + 1.0\tilde{k}^2 \right]^{-2}, \quad (7)$$

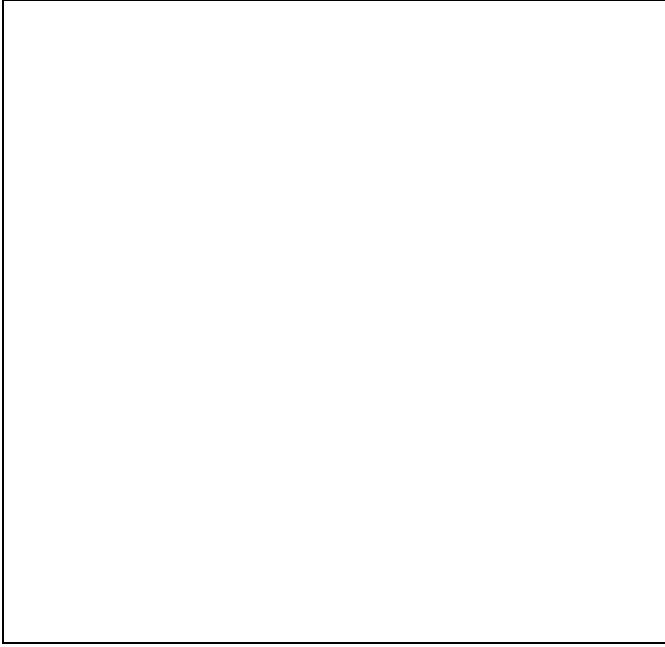


Fig. 2. The window functions $|\Psi_F|^2$ (full lines) and $|\Psi_C|^2$ (dashed) for $\Omega_0 = 1$ and sharp-edge beams, compared to some single-harmonic window functions of Scharf and Lahav (1993) (dash-dotted) and to a few forms of $k^3 P(k)$ (dotted lines). For $|\Psi_C|^2$ the curves refer to $\gamma = 2.24^\circ$ and 17.9° ; for $|\Psi_F|^2$ the curve $\gamma = 71.7^\circ$ is added. In both cases the lowest curves correspond to largest values of γ for the (arbitrarily chosen) relative normalization. The single-harmonic functions refer to $l = 4, 10$ and 40 , and are computed for the 'optimal weighting scheme' with $\Omega_0 = 0.5$, as described by Scharf and Lahav. The spectra of HDM models (labelled by H45 and H52) correspond to $h\lambda_0 = 45$ and 52.5 Mpc respectively, and those of CDM models (labelled by C50 and C15) to $\Omega_0 h = 0.50$ and 0.15

where $\tilde{k} = S(\Omega_0)k/(3000 \cdot \Omega_0 h)$. In this case the relevant parameter is $\Omega_0 h$, that we let vary in the range $(0.1 - 1)$. The corresponding peak wavelength is given by $h\lambda_0 \simeq 52(\Omega_0 h)^{-1}$ Mpc. All of the above continuous spectra are so adjusted as to reproduce the standard Harrison-Zeldovich slope at large scales and exhibit a maximum. For sharply peaked spectra, which include HDM (but not CDM) models, only the location of this maximum is really important. Thus the small-scale behaviour in Eq. (6), theoretically predicted by simple modeling of dissipative processes in hot matter, can be easily changed without affecting our conclusions. (This was tested investigating the sharply-peaked two-power spectra.) Although one can argue that Eq. (6) cannot reproduce such astronomical data as the galaxy correlation function on scales of tens of Megaparsec (see e.g. Guzzo et al. 1991), it is the simplest one can imagine and turns out to pass our tests quite well. Also, for the best fitted parameters arising from the tests it gives reasonable values of $b\sigma_8$.

For each model we calculated 300 harmonic amplitudes, in order to provide reliable results down to small angular scales. We then derived both the squared fluctuation in the source number per unit solid angle (for two-beam experiments) and the angular correlation function smeared over finite beamwidths, which are respectively given by the equations

$$\frac{\Delta N_{\text{rms}}^2(\gamma, \sigma)}{\langle N \rangle^2} = \frac{1}{2\pi} \sum_{\ell} a_{\ell}^2 F_{\ell}^2(\sigma) [1 - P_{\ell}(\cos \gamma)] \quad (8)$$

and

$$C(\gamma, \sigma) = \frac{1}{4\pi} \sum_{\ell} a_{\ell}^2 F_{\ell}^2(\sigma) P_{\ell}(\cos \gamma), \quad (9)$$

with γ the angular separation of beam centers (beamthrow), σ the effective beamwidth, and P_{ℓ} the Legendre polynomials. The coefficients $F_{\ell}(\sigma)$ are affected by the beam angular response and are well known for both Gaussian and sharp-edge beams. In this paper any theoretical results based on Eqs. (8) and (9) refer to sharp-edge circular beams, for which σ denotes the angular diameter. Equation (8) was used to evaluate ΔN_{rms} with $\sigma = \gamma$, while using (9) σ is kept fixed. In both cases we checked that calculations are accurate down to $\gamma \simeq 1^\circ$, while at $\gamma \simeq 0.5^\circ$ we would need more harmonic amplitudes.

Although the similarity of Eqs. (8) and (9) seems to imply that these two tests are quite equivalent, this is not the case. In the limiting case $\sigma = 0$, the discrete-noise terms give a vanishing contribution to $C(\gamma, \sigma)$ because $\sum_{\ell} a_{N_{\ell}}^2 P_{\ell}(\cos \gamma) = 0$ for $\gamma \neq 0$, and for the reasons explained in Fabbri (1992) any dependence on the parameter bV disappears. For finite values of σ this is no more strictly true, but the test based on the shape of $C(\gamma, \sigma)$ remains quite insensitive to bV .

A question which is very important for the main issue of our paper is, how length scales are weighted in Eqs. (8) and (9). Since $\Delta N_{\text{rms}}^2(\gamma, \sigma)$ and $C(\gamma, \sigma)$ depend linearly on a_{ℓ}^2 , which in its turn is a linear function of $P(k)$, it is possible to define two window functions Ψ_F and Ψ_C such that the cosmic-structure contributions to the above quantities are expressed as $(2/\pi) \int k^2 P(k) |\Psi_{F,C}|^2 dk$. [Cf. Eq. (8) of Scharf and Lahav (1993).] From Eqs. (4), (8) and (9) we get

$$|\Psi_F(k, \gamma, \sigma)|^2 = \frac{1}{2\pi(k^2 - 4K)^2} \sum_{\ell} (2\ell + 1) A_{\ell}^2 F_{\ell}^2(\sigma) [1 - P_{\ell}(\cos \gamma)] \quad (10)$$

and

$$|\Psi_C(k, \gamma, \sigma)|^2 = \frac{1}{4\pi(k^2 - 4K)^2} \sum_{\ell} (2\ell + 1) A_{\ell}^2 F_{\ell}^2(\sigma) P_{\ell}(\cos \gamma). \quad (11)$$

Figure 2 reports some results for $|\Psi_F|^2$ and $|\Psi_C|^2$ in critical-density models which illustrate general features. (For consistency with beamwidths used in our tests, we set $\sigma = \gamma$ and $\sigma = 2.24^\circ$, respectively, for such calculations.) It appears that small scales are weighted in two of our tests less than in the work of Scharf and Lahav (1993) using the 2-Jy IRAS survey. This is due to the statistical bias of the IRAS *redshift* survey including 2650 objects. Generally speaking, we expect a large, flux-limited sample to include more far-away sources than a redshift survey. Both $|\Psi_F|^2$ and $|\Psi_C|^2$ increase monotonically with wavelength. The actual contribution of a length scale to the signal depends on the spectrum and can be estimated as $k^3 |\Psi_{F,C}|^2 P(k)$. For instance, for rms fluctuations in the angular range $8^\circ - 35^\circ$ the signals reach their maxima at $\lambda \approx 35 - 50 h^{-1}$ Mpc for a HDM spectrum with $\lambda_0 = 50 h^{-1}$ Mpc, and at $\lambda \approx 45 - 70 h^{-1}$ Mpc for a CDM spectrum with $\Omega_0 h = 0.5$. For the same models, the signals fall to 10% of their maxima at $\lambda \approx 7 - 17 h^{-1}$ Mpc, i.e. around the boundary of the linear region, and decrease very rapidly at smaller scales. Thus nonlinear disturbances are small.

We further consider the number of local maxima in the density of sources over the sky. We define $N_{\text{peak}}(\sigma, T)$ as the number of peaks higher than a threshold T , counted in the source distribution after smoothing by a Gaussian beam with dispersion σ . Following Bond and Efstathiou (1987) we take the threshold height T in units of $\sqrt{C(O, \sigma)}$. The peak statistics is described by

$$N_{\text{peak}}(\sigma, T) = \frac{f(\gamma_*^2, \sigma, T)}{(2\pi)^{\frac{3}{2}} \theta_*^2}, \quad (12)$$

$$\theta_*^2 = \left[2 \sum_{\ell} \ell(\ell+1) a_{\ell}^2 F_{\ell}^2 \right] \left[\sum_{\ell} (\ell-1)\ell(\ell+1)(\ell+2) a_{\ell}^2 F_{\ell}^2 \right]^{-1}, \quad (13)$$

and

$$\gamma_*^2 = \left[\sum_{\ell} \ell(\ell+1) a_{\ell}^2 F_{\ell}^2 \right]^2 \left[\sum_{\ell} a_{\ell}^2 F_{\ell}^2 \right]^{-1} \left[\sum_{\ell} (\ell-1)\ell(\ell+1)(\ell+2) a_{\ell}^2 F_{\ell}^2 \right]^{-1}, \quad (14)$$

where the function f was calculated by Fabbri (1992) from the theory of Bond & Efstathiou (1987), and F_{ℓ} now pertains to Gaussian beams. Inspection of Eqs. (12-14) shows a highly non-linear dependence on a_{ℓ}^2 , so that it is not possible to define a window function. However, the strong weight given to higher order harmonics in Eqs. (13) and (14) proves that perturbations with small λ must have a strong bearing on the statistics for small beamwidths, so that we expect to be able to provide a lower limit to

a dominating scale by this test. Taking advantage of 300 harmonic amplitudes allowed us to evaluate N_{peak} accurately down to $\sigma \simeq 1^\circ$. Since now σ denotes a beam dispersion rather than a diameter, the investigation of small scales is limited somewhat more strongly than for other quantities.

3. Data Analysis

We used a galaxy sample based on the IRAS Point Source Catalog, Version II, including sources at $60 \mu\text{m}$ in the flux interval $0.6\text{--}20$ Jy. The galaxies were selected basically using the same criteria as in Strauss et al. (1990), but we also set the lower flux limit to 0.6 Jy, the completeness limit of the IRAS survey (Yahil et al. 1986), and extended the region of avoidance around the galactic plane to $\pm 10^\circ$. To reduce the residual contamination we also excluded other sky regions after source binning; see below. This sample differs from the one of Fabbri and Natale (1993), not only for the higher number of sources but also for a different calibration in Version II of the Catalog, leading to smaller spectral indexes of the sources. The average spectral index calculated from fluxes at 60 and $25 \mu\text{m}$ is -1.44 , and the one from fluxes at 60 and $100 \mu\text{m}$ is -1.35 . For the theoretical modelling in Sect. 2 we adopted the mean value -1.395 , but the results are quite insensitive to this choice.

Sources were collected in bins spanning equal intervals Δl (i.e., in Galactic longitude) and $\Delta(\sin b)$ (in the sine of Galactic latitude). We considered three resolution levels leading to three maps with 128×64 , 256×128 and 512×256 bins, respectively, over the entire celestial sphere. An effective angular diameter σ_b such that $(\pi/4)\sigma_b^2 = \Delta l \Delta(\sin b)$ can be defined for the bins. For the above resolution levels we have $\sigma_b = 2.24^\circ$, 1.12° and 0.56° , respectively. For the purpose of our analysis clean bins with a vanishing number of sources are quite significant, but we must exclude regions contaminated by galactic emission or not sufficiently observed during the survey. Hence to each source map we applied a mask excluding bins which are (i) not observed at least twice in the survey, or (ii) contained within $\pm 10^\circ$ around the galactic plane, or (iii) confused due to large number of sources (such as the Orion complex, Taurus and Ophiuchus star forming regions, the Large and Small Magellanic Clouds), or (iv) contaminated by cirrus emission. Figure 3 gives the map of our full sample of 12511 sources, obtained by using the above mask. By means of this procedure, we constructed 3 matrices with indexes (i_b, i_l) spanning Galactic coordinates, whose elements contained either the number of sources in the bins per unit solid angle $N(i_b, i_l)$ or a masking flag. These matrices will be referred to as 'bin maps' in the following.

In the first part of our analysis we compute all the possible differences between the values of $N(i_b, i_l)$ in adjacent windows and then the rms value. This amounts to calculating the quantity $\Delta N_{\text{rms}}(\gamma, \gamma)$ of Eq. (8) for sharp-

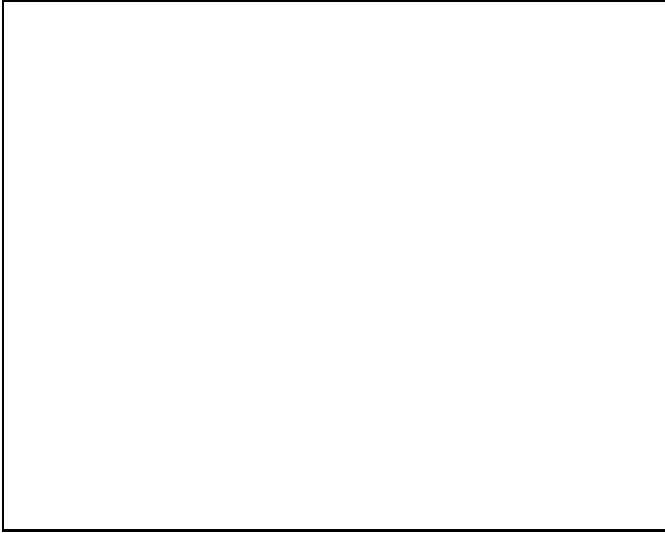


Fig. 3. Map of the 60 μm , 0.6 – 20 Jy sample

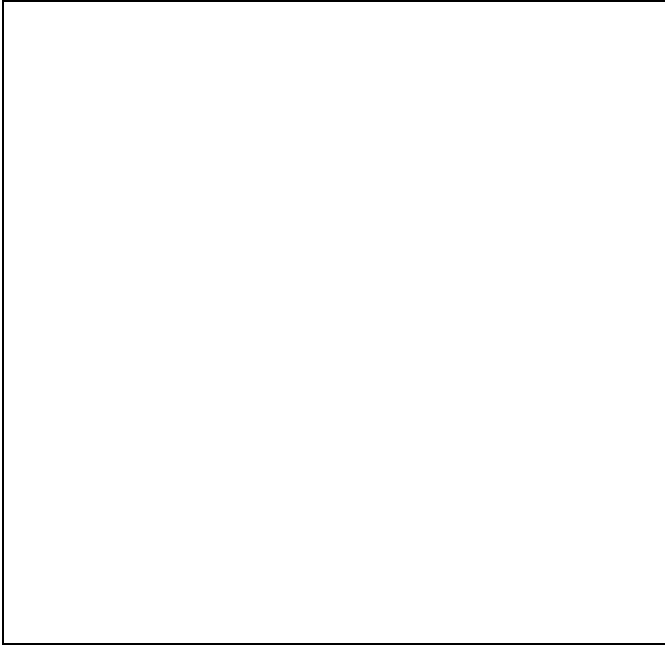


Fig. 4. Filled dots give the rms fluctuation $\Delta N_{\text{rms}}(\gamma, \gamma)$ in IRAS PSC for $\sigma_b = 2.24^\circ$ and 1.12° , with error bars computed at 1 sigma. The curves represent theoretical models with parameters selected with best fitting procedures described in Sect. 4. The full line refers to a hot-matter model with $h\lambda_0 = 60$ Mpc, $\Omega_0 = 1$, $bV = 500$ km/s. The remaining curves describe the following single-scale models: dashed, $h\lambda_0 = 40$ Mpc, $\Omega_0 = 0.7$, $bV = 400$ km/s; dotted, $h\lambda_0 = 40$ Mpc, $\Omega_0 = 1$, $bV = 500$ km/s; dash-dotted, $h\lambda_0 = 30$ Mpc, $\Omega_0 = 0.9$, $bV = 400$ km/s

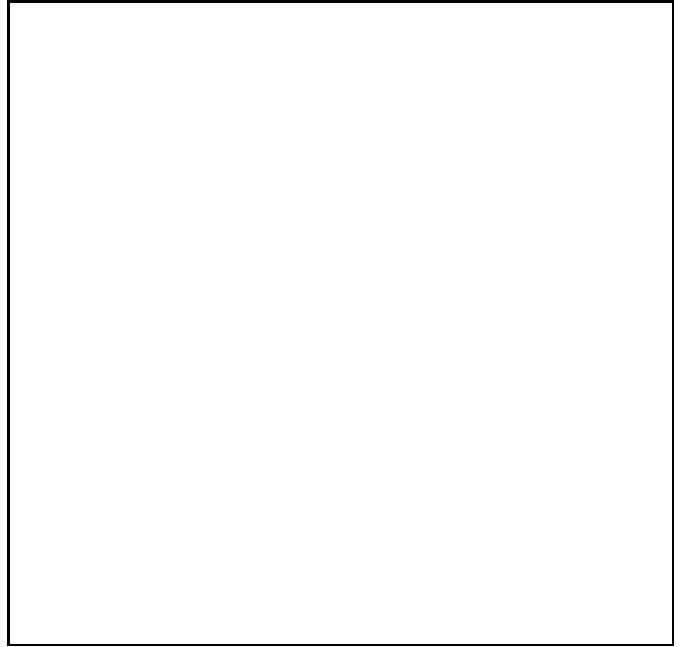


Fig. 5. Filled dots give the experimental correlation function $C(\gamma, 2.24^\circ)$ for $\sigma = \sigma_b = 2.24^\circ$, with error bars computed at 1 sigma. The full line describes a hot-matter model with $h\lambda_0 = 45$ Mpc, $\Omega_0 = 1$, $bV = 900$ km/s. Other curves refer to singlescale models: dashed, $h\lambda_0 = 30$ Mpc, $\Omega_0 = 0.9$, $bV = 700$ km/s; dotted and dash-dotted, same parameters as in Fig. 4

edge beams, except for the fact that observation windows are not circular. In order to minimize errors introduced by non-circular shapes, we maintain beam self-similarity in the generation of larger beamwidths: Starting from the above bin sizes we merge adjacent beams so that both Δl and $\Delta(\sin b)$ are doubled at each step. The effective beam diameter σ covers the range from σ_b to 71.7° at logarithmically spaced intervals. This procedure is similar to the one described in Fabbri & Natale (1990). The present analysis only differs in the treatment of masked bins in the merging process: Composed windows are now rejected when more than one bin is masked, otherwise the masked bin is filled with the average number of sources evaluated on all unmasked bins in the whole map. The results obtained for $\sigma_b = 1.12^\circ$ and 2.24° are given in Fig. 4 with error bars at 1 sigma. Ideally the two data sets should coincide up to a multiplicative factor. The figure shows that this is verified to a good accuracy: Quite small deviations arise from differences in the masks constructed at different resolutions. The data set with $\sigma_b = 0.56^\circ$ is not reported here, since it gives no new results and the first data point could not be compared to theory for the reasons explained in Sect.2.

We also computed the correlation function at $\sigma = \sigma_b = 2.24^\circ$ by means of the equation

$$C(\gamma, \sigma_b) = [n_p(\gamma, \sigma_b)]^{-1}$$

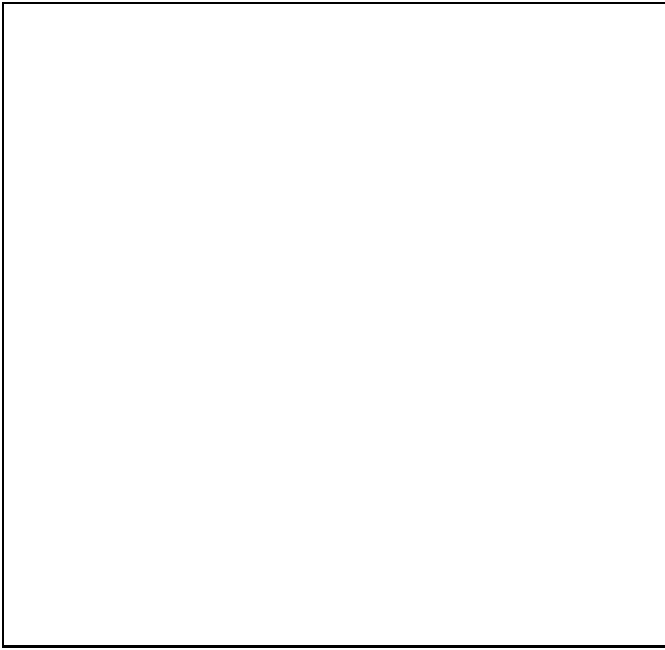


Fig. 6. The peak number vs. threshold T and Gaussian beam dispersion σ in IRAS PSC. Data points, normalized to the entire sky, are represented by mesh nodes. Three distinct meshes are given, corresponding to $\sigma_b/\sigma = 0.93$ (a), 0.47 (b), 0.23 (c)

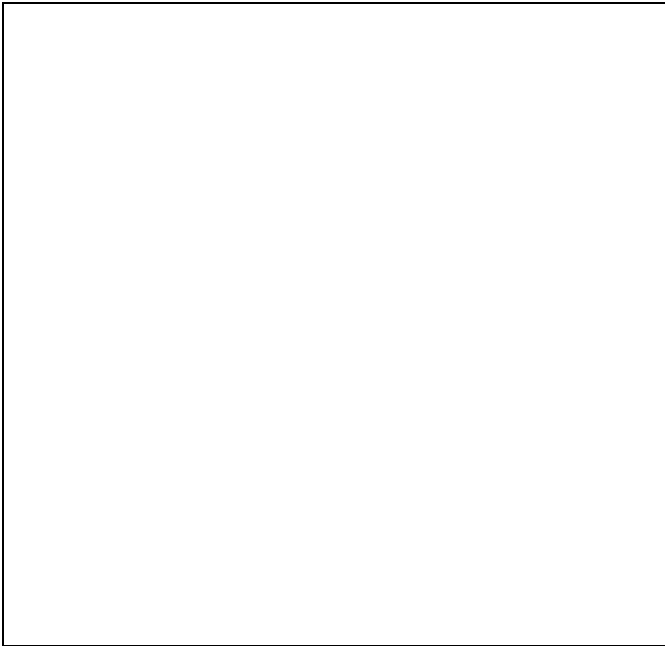


Fig. 7. The peak number for $\sigma_b/\sigma = 0.47$ from the North and South halves of the sample, labelled by N and S respectively. Data points, normalized to one half of the sky, are represented by mesh nodes



Fig. 8. The peak number vs. threshold T for $\sigma_b/\sigma = 0.47$. Filled dots represent experimental data extrapolated to the entire sky, with 1-sigma error bars, at three beamwidths $\sigma = 1.2^\circ$, 2.4° and 4.8° (with N_{peak} decreasing for increasing σ). Theoretical curves are given for single-scale models with the following parameters: full line, $h\lambda = 20$ Mpc, $\Omega_0 = 0.9$, $bV = 500$ km/s (best fit for this set of data); dashed, $h\lambda = 40$ Mpc, $\Omega_0 = 1$, $bV = 500$ km/s; dotted, $h\lambda = 30$ Mpc, $\Omega_0 = 0.9$, $bV = 400$ km/s

$$\sum [N(i_b, i_l) - \langle N \rangle] [N(j_b, j_l) - \langle N \rangle], \quad (15)$$

where the summation is performed over all pairs of beams such that the angular separation of center coordinates lies in the range $(\gamma - \frac{1}{2}\sigma_b, \gamma + \frac{1}{2}\sigma_b)$. The number of such pairs is $n_p(\gamma, \sigma_b)$, and $\gamma = n\sigma_b$ with n an integer. Masked bins are simply skipped in this computation. Now we cannot maintain self-similarity; therefore we excluded two Galactic polar cups at $|b| > 60^\circ$ where the stretching of bin shapes is strong. Figure 5 reports data in the range $\gamma \in (2.24^\circ, 24.7^\circ)$.

In order to treat the peak number statistics, we should take into account that theoretical predictions are available for smooth distributions over the celestial sphere. For any distribution of discrete sources we encounter the following problem, that moving a sharp-edge beam across the sky the detected source number varies in a discontinuous manner. Therefore we must limit ourselves to smooth beams, and in this paper we shall consider Gaussian beams. In principle, for each beam position in the sky we should weight all sources in the sample by a smoothing Gaussian factor $\exp\left[-\frac{1}{2}(\vartheta/\sigma)^2\right]$, with ϑ the source angular separation from the beam center. In practice it is more efficient

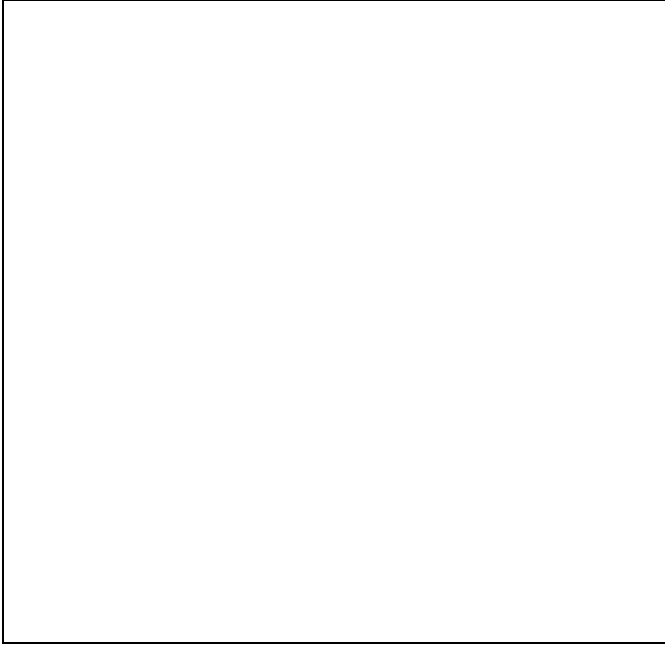


Fig. 9. The peak number vs. threshold T for $\sigma_b/\sigma = 0.23$. Filled dots represent experimental data, with 1-sigma error bars, at beamwidths $\sigma = 2.4^\circ$, 4.8° and 9.6° (with N_{peak} decreasing for increasing σ). The full line describes the single-scale model with $h\lambda = 50$ Mpc, $\Omega_0 = 0.9$, $bV = 800$ km/s (best fit for this set of data); the dashed and dotted lines refer to the same models as in the preceding figure

to replace the actual content of each bin by an effective, smoothed number of sources according to the formula

$$N_{\text{sm}}(i_{b0}, i_{l0}) = \frac{\sum N(i_b, i_l) \exp\left[-\frac{1}{2}(\vartheta_{ibil}/\sigma)^2\right]}{\sum \exp\left[-\frac{1}{2}(\vartheta_{ibil}/\sigma)^2\right]}, \quad (16)$$

where $\vartheta_{ibil} = \gamma(i_b, i_l, i_{b0}, i_{l0})$ is the angular separation between cells (i_b, i_l) and (i_{b0}, i_{l0}) . Masked bins obviously are disregarded. Now a complication arises from the fact that the measured number of peaks explicitly depends on both σ and σ_b , while theory assuming a continuous sampling of the source number-density field only predicts the σ -dependence. Therefore, to consistently compare data at varying values of σ we had to require similar geometries, i.e. equal ratios σ_b/σ . Since we considered four logarithmically spaced values of σ in the range $(1.2^\circ, 9.6^\circ)$, from our bin maps we can build three sets of data with $\sigma_b/\sigma = 0.23$, 0.47 , and 0.93 respectively. Each set includes a triplet of values of σ ; for instance, for $\sigma_b/\sigma = 0.23$ we can collect data at 2.4° , 4.8° and 9.6° taking advantage of all of our bin maps.

In practice starting from 3 original bin maps we must build 9 smoothed maps, corresponding to specific values of σ and σ_b , and in each of them we search for local maxima of the N_{sm} distribution. The search was performed comparing the source number of each bin with those of

eight contiguous bins. We handled with the presence of holes in the map developing algorithms which extended the analysis to larger neighborhoods of potential maxima. The presence of very few uncertain cases does not affect our results. The identified peaks were then normalized to the rms source-number fluctuation calculated for each smoothed map, and the distribution $N_{\text{peak}}(\sigma, T)$ was computed for 7 equally spaced values of T between 0.1 and 1.6. Since the number of peaks should then be extrapolated to the whole sky, we have to evaluate the effective area associated to the distribution of detected peaks. We adopt two procedures: (a) We only include sky bins connected to the two big unmasked continents at $|b| > 10^\circ$ and surrounded by no more than 5 masked bins, and (b) we accept all unmasked bins.

Figure 6 gives $N_{\text{peak}}(\sigma, T)$, extrapolated to the whole sky from the entire set of unmasked bins using the first method above. Since only data sets with fixed σ_b/σ are homogeneous, the figure shows 3 distinct meshes. For the case $\sigma_b/\sigma = 0.93$ only two values of σ are considered because data at $\sigma = 0.6^\circ$ could not be compared with theory. Accepting all unmasked bins for the computation of areas slightly lowers the peak numbers, but this has no important effect as will be seen in Sect. 4. Figure 7 reports $N_{\text{peak}}(\sigma, T)$ for the case $\sigma_b/\sigma = 0.47$, derived from the North and South halves of the sample. In this figure the peak number is extrapolated to one half of the sky. Error bars at 1 sigma are evaluated as $\Delta N_{\text{peak}} = \sqrt{N_{\text{peak}}/f_u}$, with f_u the unmasked sky fraction. Such errors are reported in Figs. 8 and 9.

4. Results of Best Fits

For each of our tests we basically followed the same procedure which can be outlined as follows. After selecting values for the parameters describing the source properties, we are left with two free parameters related to cosmic inhomogeneities, i.e. the products $h\lambda$ (or $h\lambda_0$) and bV . For single-scale models one more free parameter is the cosmic density parameter Ω_0 ; for HDM models we set $\Omega_0 = 1$, and for CDM models the spectral properties only depend on the shape parameter $\Omega_0 h$. For each parameter set we first minimize χ^2 with respect to a normalization factor, which in the ΔN_{rms}^2 and $C(\gamma, \sigma)$ tests determines the normalization of $P(k)$. For the peak statistics this factor should not be fitted in the ideal case of a pointlike sampling of a continuous field, namely for $\sigma_b/\sigma \rightarrow 0$, but in our case σ_b/σ can be as large as 0.93, and we have no warrant that theoretical predictions should reproduce finite-bin data exactly. However the normalization factor turned out to be usually close to unity (within $\sim 10\%$), and it was always so in the neighborhoods of the absolute minima. We then obtain 2- or 3-dimensional χ^2 grids, in which we search for χ_{min}^2 . Statistical errors on each parameter are calculated projecting out the extremal points of $(\chi_{\text{min}}^2 + 1)$ contours on the coordinate axes of two-parameter planes, after one

more minimization with respect to the third, unplotted parameter when available. The errors quoted in the following tables are quadratic combinations of such 1-sigma errors and grid half spacing.

4.1. Single-scale models

For single-scale models, adopting the optimal source parameters we calculated a 3-dimensional lattice of equally spaced points in the ranges $h\lambda = 10 - 100$ Mpc, $\Omega_0 = 0.1 - 1$ and $bV = 100 - 900$ km/s. Table 1 lists fitted parameter values that we obtained from several tests, as well as χ^2_{\min} compared to the number of degrees of freedom. Since errors on Ω_0 often exceeded the range investigated, we enclosed the best values within parentheses to declare their loss of significance.

Results reported in the table for the rms fluctuation tests (denoted by the letter F) refer to two beamthrow ranges, $1.12^\circ - 35.8^\circ$ and $2.24^\circ - 71.7^\circ$, and two values of σ_b . It was especially important to check a possible dependence of the best-fitted length scale on the beamthrow range. No difference appears in the quoted best values of $h\lambda$, but χ^2_{\min} is high in the upper range for the difficulty of fitting the data point at 71.7° . All of the rms fluctuation and correlation function data (see the fourth row in the table) are consistent with $h\lambda \simeq 30 - 40$ Mpc and $bV \simeq 300 - 500$ km/s. The parameter bV is correlated to Ω_0 ; if we assume $\Omega_0 = 1$ (which is not required by our data) we can also derive a preferred range $bV \simeq 400 - 500$ km/s. Results from the peak statistics reported at rows 5-10 of the table (denoted by the letter P) are associated to a beamwidth value. Each entry is in fact obtained using 3 beamwidths (of which the label value is the geometric mean) referring to data points with a single value of σ_b/σ . Thus for instance, the cases labelled by P2.4°(a) and P2.4°(b) use each 21 data points with $\sigma = 1.2^\circ, 2.4^\circ$ and 4.8° and $\sigma_b/\sigma = 0.47$. The letters a and b refer to the methods for extrapolating the number of peaks to the whole sky described in Sect. 3. The test combining all of our N_{peak} data is denoted by the full range $1^\circ - 10^\circ$. Entries in the 6th and 7th row show that consistent results were obtained for the North or South hemispheres (which was verified for N_{peak} tests at all beamwidths). We do not report results for the self-similar case with $\sigma_b/\sigma = 0.93$ because no significant result could be found after exclusion of data with $\sigma = 0.6^\circ$. Inspection of the table shows that in all cases we consistently find $h\lambda = 20 - 30$ Mpc and 50 Mpc for smaller and larger beamwidths, respectively. The former can be regarded as a safe lower limit to a preferred scale.

Figure 10 gives a few contours in the $(h\lambda, bV)$ plane corresponding to $\chi^2_{\min} + \Delta\chi^2$, with $\Delta\chi^2 = 2.3$ and 6.17, which for a Gaussian field should delimit the ellipses at confidence levels of 1 and 2 sigmas, respectively [cf. Press et al. (1988), Chapt. 14]. The figure shows that contours for the P tests do not overlap at 2 sigmas, since the

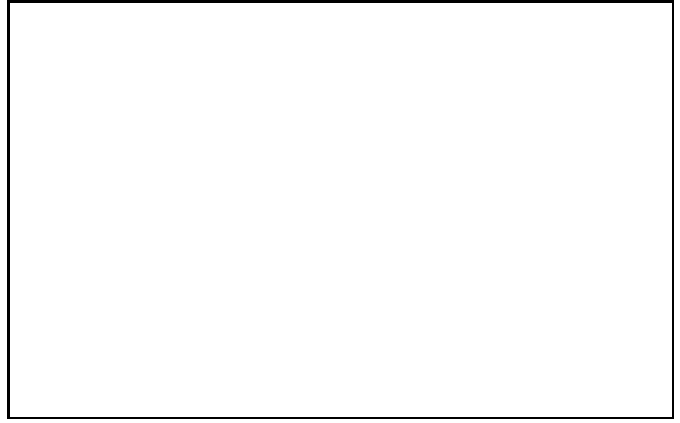


Fig. 10. The χ^2 contours in the $(h\lambda, bV)$ plane corresponding to levels 2.30 (full lines) and 6.17 (dashed) above χ^2_{\min} , for a few tests based on single-scale models. The specific tests involved are identified by the curve labels, which are also used in Table 1 and explained in the text

preferred length scale show some dependence on angular scale. However, all of the other tests (included those not reported in the Figure) provide intermediate results.

Finally, since as already remarked N_{peak} weights high-order harmonics much more strongly than $\Delta N_{\text{rms}}(\gamma, \gamma)$ and $C(\gamma, \sigma)$ do, we treated N_{peak} data as quite independent from the other two sets of data. This allows us combining couples of tests, simply summing up the respective χ^2 fields. Entries labeled as F+P and C+P in the last two rows of Table 1 respectively combine data from the $P1^\circ - 10^\circ$ (a) case with data from $F1^\circ - 72^\circ(1^\circ)$ and $C2^\circ - 25^\circ$. The resulting χ^2_{\min} are only slightly higher than the sums of minima in the component fields, which obviously refer to different values of the fitted parameters: This fact is due to the slow variations of χ^2 around the minima. Therefore the rather large values of χ^2_{\min} in Table 1, which emphasize the limits of the single-scale approximation, mainly arise from some difficulties that the models encounter in each of our basic tests.

4.2. Continuous spectra

In the case of continuous-spectrum models after minimization of χ^2 with respect to the normalization factor we built 2-dimensional grids in the plane $(h\lambda_0, bV)$ or $(\Omega_0 h, bV)$ for HDM and CDM respectively.

For HDM models the range limits were the same as for single-scale models, but the 2-dimensional χ^2 grid was not equally spaced in the $h\lambda_0$ direction. (The finest spacing, adopted around the χ^2 minima, was 2.5 Mpc.) Table 2 reports the results obtained in a subset of our best fitting procedures, which is sufficient to illustrate our findings. The table shows that the values of χ^2 are very close to the numbers of degrees of freedom for all of the reported tests. The best fitted values of $b\sigma_8$, derived both from

Table 1. Best fit parameters for single-scale models

Case [†]	$h\lambda$ (Mpc)	Ω_0	bV (km/s)	χ^2_{\min}/DOF
F1° – 36°(1°)	40^{+8}_{-12}	(1.0)	500^{+50}_{-360}	4.1/2
F1° – 72°(1°)	40^{+15}_{-7}	0.7 ± 0.5	400^{+180}_{-130}	15.2/3
F2° – 72°(2°)	40^{+16}_{-8}	0.7 ± 0.5	400^{+150}_{-130}	14.5/2
C2° – 25°	30^{+12}_{-6}	(0.9)	700^{+240}_{-600}	21.1/7
P2.4°(a)	20^{+13}_{-5}	(0.9)	500 ± 410	14.2/17
P2.4°(a, N) [§]	30^{+21}_{-9}	(1.0)	300^{+280}_{-240}	15.6/17
P2.4°(a, S) [§]	20^{+15}_{-5}	(0.8)	600 ± 350	20.8/17
P2.4°(b)	20^{+12}_{-5}	(0.9)	500^{+400}_{-410}	14.6/17
P4.8°(a)	50^{+17}_{-8}	(0.9)	800^{+130}_{-530}	24.0/17
P4.8°(b)	50^{+16}_{-8}	(0.9)	800^{+130}_{-530}	24.5/17
P1° – 10°(a) [‡]	30^{+10}_{-7}	(0.8)	400^{+240}_{-300}	30.0/22
F+P *	40^{+9}_{-10}	1.0 ± 0.6	500^{+50}_{-230}	47.3/27
C+P *	30^{+10}_{-6}	(0.9)	400^{+310}_{-290}	51.2/32

[†] Label F denotes rms fluctuation tests in the specified beamthrow range; rounded-off bin size is within parentheses. C means correlation test in the specified beamthrow range; bin size is 2.24°. P marks peak number tests for triplets of σ around quoted values. For the meaning of (a) and (b) labels see Sect. 3.

[§] N, S = Northern and Southern half of the sky.

[‡] Full range of σ used.

* Joint tests combine P1° – 10°(a) data with F1° – 72°(1°) and C 2° – 25°, respectively.

bV and from the normalization factor of $P(k)$, are often fairly close to the 'canonical' value 0.7 (Lahav et al. 1990, Saunders et al. 1992) although there is some spreading in the results. One might have expected to find lower values of $b\sigma_8$ for HDM models; however, this is not the case because our spectra are peaked at low wavelengths. The only real limitation for so satisfactory results is the exclusion of the data point at 71.7° in the case of the rms fluctuation test. The behaviour of the HDM model represented by the full line in Fig. 4 shows how such a point spoils the quality of a fit which would otherwise be very good. In general, the quality of fits for any sharply-peaked (including single-scale and double-power) models is somewhat worse at larger angles. Thus in Fig. 5 models do not strictly follow the oscillations of $C(\gamma, 2.24^\circ)$ around $\gamma \approx 20^\circ$, and finally, all of our theoretical distributions of density peaks slightly deviate from experiment at our largest beamwidth, the measured $N_{\text{peak}}(9.6^\circ, T)$ being systematically lower than predicted for $T > 0.8$. We could not extend the analysis to angles larger than 10° because the small number of expected peaks is completely masked by Poisson noise.

For the above reasons, we performed the global test F+P for HDM combining the P1° – 10°(a) and F1° –

36°(1°) data. Contours at 1- and 2-sigma confidence levels for the F+P and C+P tests are reported in Fig. 11. These global tests appear to be somewhat complementary, setting more stringent limits on bV and $h\lambda_0$ respectively. We can satisfy both simultaneously with $bV \simeq 450 - 550$ km/s and $h\lambda_0 \simeq 45 - 55$ Mpc.

Table 3 collects results for CDM tests corresponding to those of Table 2. In all of these tests $\Omega_0 h$ is allowed to vary in the range (0.1, 1.2). However in the last column we also report χ^2_{\min} , the minimum chi-square obtained in the smaller range (0.5, 1.2). The latter range is suitable to test critical density models, letting h vary; in this case the constrained minima are always found at $h = 0.5$, but the fits are unsatisfactory with the exception of peak statistics. Allowing for low-density models the situation improves substantially: For tests involving peak statistics only, χ^2_{\min} is even slightly smaller than for hot matter. However, the chi-square minima identified by our tests are spread in the range $\Omega_0 h = 0.1 - 0.5$ and do not appear so mutually consistent as in the case of hot matter. The situation is made clear by inspection of Fig. 12: For cold matter the C+P and F+P tests allow us identifying an overlap region ($\Omega_0 h \simeq 0.4$, $bV \simeq 600$ km/s) only at a formal confidence level of 2 sigmas.

Table 2. Best fit parameters for HDM models

Case	$h\lambda_0$ (Mpc)	bV (km/s)	$b\sigma_{8V}^\dagger$	$b\sigma_{8N}^\ddagger$	χ^2_{\min}/DOF
$F1^\circ - 36^\circ(1^\circ)$	60^{+32}_{-14}	500^{+130}_{-70}	0.60	0.75	2.5/3
$C2^\circ - 25^\circ$	45^{+11}_{-4}	900 ± 560	1.14	1.23	8.3/8
$P1^\circ - 10^\circ(a)$	$42.5^{+17}_{-4.5}$	700^{+130}_{-190}	0.89	–	25.6/23
$F+P^*$	52.5^{+22}_{-7}	500^{+90}_{-60}	0.62	–	30.3/27
$C+P^*$	$45.0^{+5}_{-1.5}$	700^{+130}_{-270}	0.89	–	34.1/33

[†] Calculated from bV in the preceding column.

[‡] Calculated from the normalization factor of $P(k)$.

* Joint tests combine $P1^\circ - 10^\circ(a)$ data with $F1^\circ - 36^\circ(1^\circ)$ and $C2^\circ - 25^\circ$, respectively.

Table 3. Best fit parameters for CDM models [†]

Case	$\Omega_0 h$	bV (km/s)	χ^2_{\min}/DOF	$\chi^{*2}_{\min}/\text{DOF}$
$F1^\circ - 36^\circ(1^\circ)$	$0.10^{+0.03}_{-0.10}$	600^{+150}_{-90}	5.7/3	21.1/3
$C2^\circ - 25^\circ$	$0.50^{+0.10}_{-0.15}$	900^{+50}_{-660}	13.8/8	13.8/8
$P1^\circ - 10^\circ(a)$	$0.35^{+0.18}_{-0.15}$	900^{+150}_{-160}	23.5/23	24.9/23
$F+P^*$	$0.15^{+0.03}_{-0.15}$	600^{+160}_{-60}	35.2/27	45.6/27
$C+P^*$	$0.45^{+0.12}_{-0.13}$	900^{+130}_{-240}	38.2/33	38.8/33

[†] Starred quantities (last column) refer to best fits limited to the range $\Omega_0 h \geq 0.5$.

* Joint tests combine $P1^\circ - 10^\circ(a)$ data with $F1^\circ - 36^\circ(1^\circ)$ and $C2^\circ - 25^\circ$, respectively.

In order to decide whether our tests really argue against CDM models in low-density cosmologies, we should discuss the significance of error bars we attach to fitted parameters. The confidence regions derived from χ^2 contours stem from purely statistical errors. (Error bars quoted in Tables 1-3 also include grid spacing.) As pointed out by White, Krauss and Silk (1993) cosmic variance can be more important than instrumental noise in anisotropy experiments such as those on the cosmic background radiation. In our case the ‘instrumental’ noise (i.e., the error in counting extragalactic sources in sky bins in a definite flux interval) is negligible in front of the noise term $\Delta N(i_b, i_l) = \sqrt{N(i_b, i_l)}$, which is the source of our error bars. Cosmic variance is just this noise term. In order to check that this interpretation is correct, we attributed the standard cosmic-variance uncertainty $\Delta(a_l^2) = a_l^2 / \sqrt{l + \frac{1}{2}}$ to all of the models which best fitted any one of our tests, and derived the corresponding uncertainties Δ_{CV} on the theoretical quantities ΔN_{rms}^2 , $C(\gamma, \sigma)$ and N_{peak} . We found that our declared errors in Figs. 4-9 are typically 0.7 – 1.7 times Δ_{CV} , and this ra-

tio is larger as it must when theoretical predictions lie below experimental data points. The average ratio $\sim 1.2 \sim f_u^{-\frac{1}{2}}$ is consistent with theoretical expectation taking into account the unmasked portion of the sky.

As noted by Scaramella and Vittorio (1993), taking cosmic variance into account in the computation of the χ^2 field does not provide exactly the same results as simulations: Models predicting anisotropies larger than experiment are affected by a larger cosmic variance, and can be rejected less easily than we could infer from inspection of the χ^2 field. From these considerations and the inspection of Table 3 and Fig. 12, it follows that low-density CDM models are not clearly ruled out by our tests. However, very simple HDM models work remarkably better.

5. Discussion

The results expounded in Sect. 4 show that a common picture arises from both single-scale and HDM models. The scale $\lambda \sim 30 - 40 h^{-1}$ Mpc suggested by the former is only slightly smaller than the peak wavelength λ_0 arising from the latter (in particular, the value $45 - 55 h^{-1}$

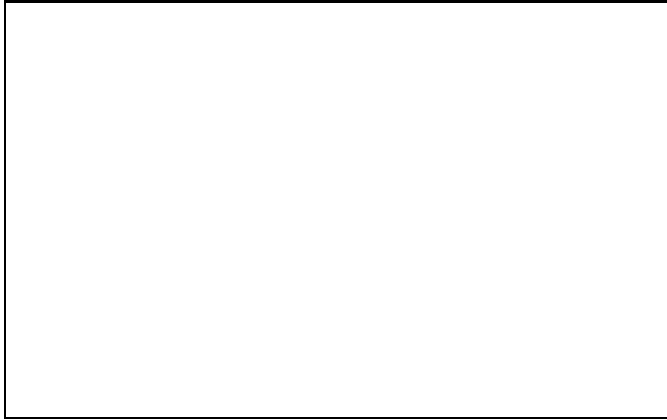


Fig. 11. The χ^2 contours in the $(bV, h\lambda_0)$ plane corresponding to levels 2.30 and 6.17 above χ^2_{\min} , for two global tests on HDM models, respectively labelled by F+P and C+P



Fig. 12. The χ^2 contours in the $(bV, \Omega_0 h)$ plane corresponding to the same levels above χ^2_{\min} as in the preceding figure, for two global tests on CDM models, respectively labelled by F+P and C+P

Mpc implied by the simultaneous consideration of the global tests). The linear component of our local velocity (in practice, the velocity of the Local Group) is estimated around $500 h^{-1}$ km/s, in agreement with current views on the large-scale velocity field, although not with inferences of about 1000 km/s (cf. Collins et al. 1986). Our basic conclusions remain unchanged for different source parameters and sharply-peaked spectral shapes provided only that IRAS sources already existed at $z \sim 0.1$. The quality of HDM fits suggests that $P(k)$ is characterized by some length scale smaller than appearing from the analyses of redshift surveys.

Possible objections to this result might involve the reliability of the sample, the ability of our tests to effectively probe the full perturbation spectrum and contamination from small, non-linear scales.

As to the first point, we are confident that our sample is reliable. Similar results (using single-scale models

and two of the present tests) were obtained from another sample derived from IRAS PSC, Version I with more conservative selection criteria (Fabbri & Natale 1990, 1993). Thus there is no chance that our results might be affected by star contamination. No problem should arise from the finite depth of the sample. Applying the peak statistics separately to the South and North halves of the sky we reduced the effective linear scale of the sample by a factor $2^{\frac{1}{2}}$, but we observed no shift of the best-fitted wavelength or the confidence regions to lower scales. Also, our models carefully take into account the flux interval of the sample, the source luminosity function and the relativistic expression of the luminosity distance; they explicitly allow for the effective depth arising from the interplay of such factors. So there is no reason why such a length scale should strongly affect our tests, nor why a spectrum like (6) should fit data better than equation (7). [In fact, the luminosity function of Saunders et al. (1990) does not even allow us identifying a length scale so sharply.] The depth of the sample could drastically affect the fittings only if it arises from a strong cutoff, totally independent of the above factors and effective at redshifts < 0.1 . There is no evidence for such a cutoff. We previously studied the effect of varying the lower flux limit on Version I of PSC and found no effects of this kind (Fabbri & Natale 1990). We further notice that Jing & Valdarnini (1993) use the redshift field of 2-Jy IRAS galaxies to infer a peak wavelength of $\sim 300 h^{-1}$ Mpc. The median depth of their sample is quite smaller than ours. Thus the different results arise from the different techniques, not from peculiarities of our sample.

It is therefore important to notice that the shape of the window functions which can be defined for our tests do not weight small length scales to a pathological extent; actually they weight them less than a 2-dimensional analysis based on IRAS redshift survey (Scharf and Lahav 1993).

All of the above considerations cannot prove of course that our best value for λ_0 should be the location of the absolute maximum of $P(k)$. We are aware that best-fit procedures are not equivalent to directly constructing the shape of $P(k)$ from data. This consideration is especially important because we find that our tests, when applied to CDM models, point to larger length scales. This apparently strange result may also be linked to the fact that in 2-dimensional analyses length scales are smeared out; under this respect 3-dimensional studies (e.g. Feldman et al. 1994) are superior. However, the quality of our HDM low-wavelength fits and the arguments discussed in the Introduction makes us suspect that current spectra obtained from redshift catalogs may not represent the correct $P(k)$ in real space very accurately. Although there is a qualitative agreement between spectra inferred from visible and IRAS galaxies and clusters, a close inspection of the papers by Fisher et al. (1993), Einasto et al. (1993) and Jing & Valdarnini (1993) shows significant differences

between the spectra proposed by these authors. A conservative interpretation of our results is that at least a spectral feature should exist, not detected in the above works. Strictly speaking, a local peak around $45h^{-1}$ Mpc appears in Fig. 5 of Jing & Valdarnini, but we believe its strength is too weak to justify our findings. A recent work by Baugh & Efstathiou (1993) studies the 2-dimensional correlation function in the APM survey and recovers $P(k)$ by the method of Lucy (1974). Their spectrum rises above a power law around $30h^{-1}$ Mpc and appears to be peaked at $100h^{-1}$ Mpc. Although the authors find that their results may be compatible with previous work, still they declare that the discrepancy showed by their Fig. 11 is disturbing.

In our opinion the support for a steady increase of $P(k)$ up to very large wavelengths is not overwhelming. [Difficulties may arise also in connection with data on the anisotropies of the cosmic background radiation (Fabbri & Torres 1994)]. The problems arising from the comparison of results found with different techniques may indicate that the cosmic spectrum is more complicated than the smooth theoretical shapes appearing in the current literature.

Acknowledgements. We wish to thank M. T. Dibari for useful discussions on IRAS PSC. This work is partially supported by Agenzia Spaziale Italiana under Contract # 92RS64, and by the Italian Ministry for the University and Scientific and Technological Research (Progetti Nazionali e di Rilevante Interesse per la Scienza).

References

- Bahcall, N.A., Cen, R., Gramann, M. 1993, ApJ 408, L77
 Baugh, C.M., Efstathiou, G. 1993, MNRAS 265, 145
 Bond, J. R., Efstathiou, G. 1987, MNRAS, 226, 407
 Clowes, R., Savage, A., Wang, G., et al. 1987, MNRAS 229, 27P
 Collins, C.A., Joseph, R.D., Robertson, N.A. 1986, Nat, 320, 506
 Davis, M., Peebles, P. J. E. 1983, ApJ 267, 465
 Davis, M., Summers, F.J., Schlegel, 1992, Nat 359, 393
 Efstathiou, G., Bond, J.R., White, S. 1992, MNRAS 258, 1p
 Einasto, J., Gramann, M., Saar, E., et al. 1993, MNRAS 260, 705
 Fabbri, R. 1988, ApJ, 334, 6
 Fabbri, R. 1992, A&A, 259, 1
 Fabbri, R., Natale, V. 1990, ApJ, 363, 3
 Fabbri, R., Natale, V.: 1993, A&A, 267, L15
 Fabbri, R., Torres, S. 1994, Report FS#941U
 Feldman, H.A., Kaiser, N., Peacock, J.A. 1993, ApJ 426, 23
 Fisher, K. B., Davis, M., Strauss, M. A., et al. 1993, ApJ 402, 42
 Guzzo, L., Iovino, A., Chincarini, G., et al. 1991, ApJ 382, L5
 Jing, Y. P., Valdarnini, R. 1993, ApJ 406, 6
 Lahav, O., Nemirof, R.J., Piran, T. 1990, ApJ 350, 119
 Lawrence, A., Walker, D., Rowan-Robinson, M., et al. 1986, MNRAS, 219, 687
 Lucy, L.B. 1974, AJ 79, 745

- Press, W.H., Flannery, B.P., Teukolsky, S.A., et al. 1988, Numerical Recipes, Cambridge University Press, Cambridge
 Rowan-Robinson, M., Lawrence, A., Saunders, W., et al. 1990, MNRAS, 247, 1
 Saunders, W., Rowan-Robinson, M., Lawrence, et al. 1990, MNRAS, 242, 318
 Saunders, W., Rowan-Robinson, M., Lawrence, A. 1992, MNRAS 258, 134
 Scaramella, R., Vittorio, N. 1993, MNRAS 263, L17
 Scharf, C.A., Lahav, O. 1993, MNRAS 264, 439
 Strauss, M. A., Davis, M., Yahil, A., et al. 1990, ApJ 361, 49
 Taylor, A.N., Rowan-Robinson, M. 1992, Nat 359, 396
 Torres, S., Fabbri, R., Ruffini, R. 1994, A&A (in press)
 Villumsen, J.V., Strauss, M. A. 1987, ApJ, 322, 37
 Vogeley, M.S., Park, C., Geller, M.J., et al. 1992, ApJ 391, L5
 White, M., Krauss, L.M., Silk, J. 1993, ApJ 418, 535
 Yahil, A., Walker, D., Rowan-Robinson, M. 1986, ApJ, 301, L1

This figure "fig1-1.png" is available in "png" format from:

<http://arxiv.org/ps/astro-ph/9412065v1>

This figure "fig2-1.png" is available in "png" format from:

<http://arxiv.org/ps/astro-ph/9412065v1>

This figure "fig3-1.png" is available in "png" format from:

<http://arxiv.org/ps/astro-ph/9412065v1>

This figure "fig4-1.png" is available in "png" format from:

<http://arxiv.org/ps/astro-ph/9412065v1>

This figure "fig1-2.png" is available in "png" format from:

<http://arxiv.org/ps/astro-ph/9412065v1>

This figure "fig2-2.png" is available in "png" format from:

<http://arxiv.org/ps/astro-ph/9412065v1>

This figure "fig3-2.png" is available in "png" format from:

<http://arxiv.org/ps/astro-ph/9412065v1>

This figure "fig4-2.png" is available in "png" format from:

<http://arxiv.org/ps/astro-ph/9412065v1>

This figure "fig1-3.png" is available in "png" format from:

<http://arxiv.org/ps/astro-ph/9412065v1>

This figure "fig2-3.png" is available in "png" format from:

<http://arxiv.org/ps/astro-ph/9412065v1>

This figure "fig3-3.png" is available in "png" format from:

<http://arxiv.org/ps/astro-ph/9412065v1>

This figure "fig4-3.png" is available in "png" format from:

<http://arxiv.org/ps/astro-ph/9412065v1>